Materials Science & Engineering A 858 (2022) 144061

Contents lists available at ScienceDirect

Materials Science & Engineering A

journal homepage: www.elsevier.com/locate/msea

Temperature-dependent formation of gradient structures with anomalous hardening in an Al–Si alloy

Xiaolong Ma [a,*], Matthew Olszta [a], Jia Liu [a], Miao Song [b], Mayur Pole [b], Madhusudhan R. Pallaka [a], Joshua Silverstein [a], Julian Escobar [b], Arun J. Bhattacharjee [b], Sundeep Mukherjee [c], Arun Devaraj [b], Bharat Gwalani [b,**,1]

[a] Energy and Environment Directorate, Pacific Northwest National Laboratory, Richland, WA, 99352, USA
[b] Physical and Computational Science Directorate, Pacific Northwest National Laboratory, Richland, WA, 99352, USA
[c] Department of Materials Science and Engineering, University of North Texas, Denton, TX, 76201, USA

ARTICLE INFO

Keywords:
Gradient structure
Temperature effect
Gradient steepness
Surface severe deformation
Oxide dispersion strengthening

ABSTRACT

The temperature effect on forming gradient structure in an Al–Si alloy during surface severe deformation is studied in this report. The intermediate temperature (473 K) produces the steepest gradient structure by an anomalous hardening on the top layer compared to lower (300 K) and higher temperature (673 K) counterparts. Our analysis shows profuse aluminum oxide particles in the top layer of the gradient structure under 473 K lead to anomalous hardening by oxide-dispersion strengthening. The counterintuitive enhancement of strengthening at the intermediate temperature is explained by the dynamic interplay between thermal-driven, mechanical-aided oxidation and the wear-induced loss of surface materials as a function of temperature, which yields a critical processing temperature to achieve the steepest gradient structure.

1. Introduction

Heterogeneous microstructure design through gradual changes in grain size, defect density, texture, etc., has garnered extensive interest in the community during the past decades [1–3]. There is a growing research interest in gradient structured (GS) pure metals and alloys ranging from conventional metals such as Cu and steels to emerging multi-principal element alloys [4–6]. Compared to the conventionally homogeneous counterparts, the GS metals were reported to exhibit extraordinary mechanical properties, including outstanding strength-ductility synergy [2,7], enhanced fatigue resistance [8], and remarkable wear resistance [9]. Fundamentally, those superior mechanical properties are intrinsically associated with the microstructure characteristics of GS, such as the gradient steepness and the volume fraction of GS in the whole material [10,11]. For example, to boost the strength in GS metals while maintaining decent ductility, a sufficiently steep gradient across the spatial distribution of its microstructure is often required to induce substantial mechanical incompatibility upon plastic deformation [12,13]. It is this mechanical incompatibility that promotes the emergence of the strain/stress gradient and the storage of geometrically necessary dislocations on the fly during deformation, which is commonly believed to play an essential role in achieving the extra work hardening and the exceptional strength-ductility synergy [3,14,15].

Naturally, the microstructure characteristics of GS are determined by its fabrication route and conditions. To date, the primary fabrication method to produce bulk GS metals is surface mechanical treatment (attrition, grinding, rolling, peening) to generate gradients in the materials via severe plastic deformation [3]. Most of these fabrications were carried out at ambient temperature rather than elevated temperatures, with the main objective of suppressing the growth of most refined grains at the outermost layer to achieve a steep gradient in grain size. It is noteworthy that increasing the processing temperature may also induce microstructural evolutions benefiting the formation of a steep gradient structure, for example, partial oxidation during deformation. Forming a surface oxide layer, especially when the oxides are uniformly dispersed in the metal matrix, can provide effective strengthening [16], potentially inducing a significant mechanical

* Corresponding author.
** Corresponding author.
E-mail addresses: xiaolong.ma@pnnl.gov (X. Ma), bgwalan@ncsu.edu (B. Gwalani).
[1] Current address: Department of Materials Science and Engineering, North Carolina State University, Raleigh, NC, 27695-7907, USA.

https://doi.org/10.1016/j.msea.2022.144061
Received 21 May 2022; Received in revised form 7 September 2022; Accepted 20 September 2022
Available online 27 September 2022

incompatibility from the exterior to the interior, i.e., a steep gradient. However, the competition between the loss of grain boundary strengthening (due to grain growth) and the gain of oxide dispersion strengthening to mediate the formation of GS as a function of temperature is not well understood. In addition, the dynamical nature of the interplay between deformation and *in-situ* oxidation adds another layer of complication to comprehending the formation process of GS at different temperatures.

In this study, we investigate the formation of a GS in an Al–Si alloy by high strain cyclic shear deformation at three different temperatures. The focus is to unveil how processing temperature influences the obtained GS steepness through the dynamic interplay between the surface severe deformation and the attendant oxidation. The Al–Si alloy system, selected for this study is a popular cast binary alloy system, representing about 85–90% of the total cast Al products, and thus holds crucial significance for applications [17]. Our proof-of-concept study is applicable to a range of surface deformation-based solid-phase processing techniques that result in gradient microstructures.

2. Materials and methods

The high-purity Al-4at.%Si alloy was melted in a vacuum furnace protected with an argon atmosphere and then cast. A thin plate was cut from the cast ingot, metallographically polished using 0.02 μm colloidal silica solution. Fig. 1a presents the microstructure of this starting material, consisting of coarse dendritic grains and networks of the eutectic Al–Si phase (bright). Dry sliding and reciprocating wear tests were performed using a RTEC Universal Reciprocating Tribometer with temperature control (RTEC Instruments) to heat the stage up to 673 K through active feedback loop. A 6-mm-diameter stainless-steel counterface with a load of 1 N in ambient air and a linear speed of 200 mm/s (~14.28 cycles/s) was used in the reciprocating mode for 5000 cycles, with a stroke length of 7 mm, as sketched in Fig. 1b. The temperature was held constant for at least 30 min prior to the tribometer tests. MFT17 software was used to record the coefficient of friction (COF) and Gwyddion software was used to calculate the wear rates (dividing wear volume loss with load and the sliding distance) through analysis of white light interferometry (WLI). To reveal the steepness (in mechanical properties) of the GS obtained at various temperatures, arrays of nanoindentation testing were performed with a load of 10 mN using PB1000 (Nanovea) on the cross-sections of the gradient microstructures starting from the topmost region using 15 μm as the spacing. While not aiming to fabricate GS materials at bulk scale, the present tribological method sheds light on the fundamental understanding of processing-structure-property interrelationship that is common to complex gradient microstructures produced by surface severe deformation techniques.

The tribological deformation results in a gradation in strain distribution below the wear track, thus resulting in a GS. The gradient microstructure below the wear track was characterized using scanning electron microscopy (SEM), electron backscatter electron diffraction (EBSD), scanning/transmission electron microscopy (S/TEM), and atom probe tomography (APT). The SEM samples were prepared by mechanical polishing followed by chemical mechanical cleaning via vibrational polishing and observed using Quanta field-emission SEM (Thermo Fisher Scientific). The TEM foils and APT specimens were made from the region of interest in the wear trenches using the focus ion-beam (FIB) lift-out technique with a Quanta 200 FIB-SEM (Thermo Fisher Scientific). The foils were examined by an aberration-corrected ARM200F (JEOL) S/TEM operated at 200 kV to obtain bright-field micrographs, energy dispersive X-ray spectroscopy (EDS) data, and precession electron diffraction (PED) data. The APT analysis was conducted using a CAMECA LEAP 4000X HR equipped with an ultraviolet ($\lambda = 355$ nm) wavelength laser and a reflectron lens. The obtained data was further reconstructed to a 3D ion map using the position and time-of-flight of each individual detected ion by employing the integrated visualization and analysis software (IVAS 3.6) developed by CAMECA.

3. Results and discussion

The backscatter electron micrographs of the transverse cross-section of the wear tracks at three temperatures (300, 473, and 673 K) are shown in Fig. 1c. The cyclic tribological deformation on the surface creates the shear-zone trenches. The depth of the trenches increased with increasing temperature. Along with the increasing depth, the coefficient of friction and wear rate both demonstrate a similarly increasing trend as a function of temperature (Fig. 1d). Given the identical load and strain rate (i.e., directly measured from the

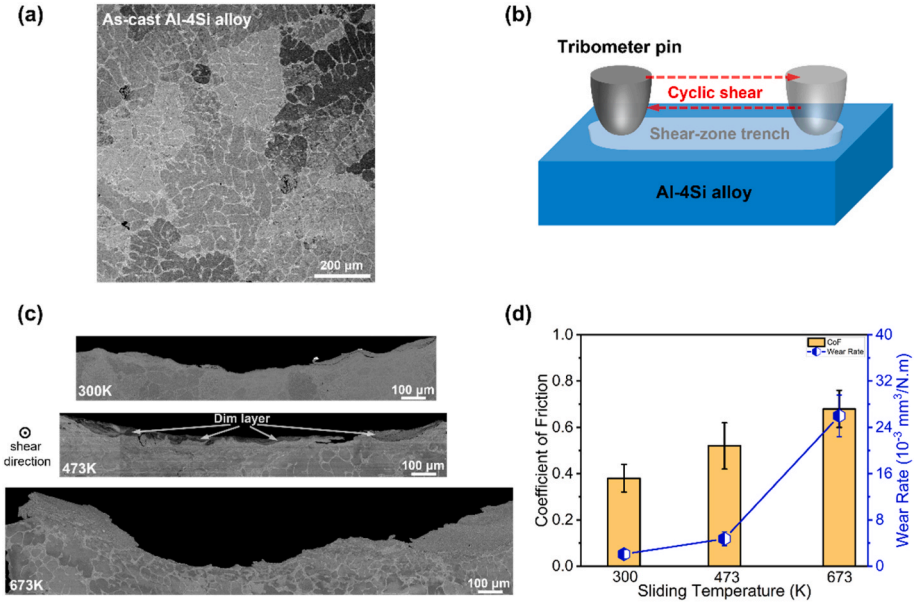

Fig. 1. (a) Backscatter electron (BSE) micrograph of the starting microstructure of the as-cast Al–4Si alloy; (b) Schematics of severe cyclic surface shear deformation at various temperatures; (c) BSE transverse cross-sectional micrographs of the shear zone trenches produced at three different temperatures (300 K, 473K, and 673 K); (d) Coefficient of friction and wear rate measured during the cyclic shear deformation on the samples at different temperatures.

reciprocating speed of the counterface), the thermal softening with increasing temperature is expected to facilitate the deformation at elevated temperatures by lowering the barrier for dislocation motion, thus increasing the wear volume loss of the material. Below the trench, the tribological shear strain decays with increasing depth into the material. The severe strain at the top imparts profuse dislocations and could lead to substantial grain refinement through dynamic recrystallization for Al even at room temperature [18]. Hypothetically, temperature will further mediate the recrystallization process to form GS with different characteristics. Notably, at the top of the GS in the 473 K tested sample is a discontinuous and dim greyish contrast layer with a variable thickness (0–70 μm), as labeled in Fig. 1c. This appreciable layer with prominent dark contrast is not observed in either the lower (300 K) or the higher (673 K) processing temperatures, suggesting a microstructural evolution containing chemistry change unique to the intermediate-temperature range.

The GS steepness is of most interest in this study. To characterize different steepness levels in GS produced at three temperature conditions, nanoindentation hardness profiles to a depth of 120 μm were obtained, as shown in Fig. 2a. Surprisingly, the steepest hardness profile is achieved at the intermediate temperature (473 K) with an almost tripled hardness at the topmost 10 μm compared to the benchmark value of the base material. An inset optical micrograph of the indent arrays on this sample is provided in Fig. 2a, also featuring the much smaller indent size on the top two rows. On the contrary to this, at the lower (300 K) and higher (673 K) temperatures, the cyclic tribological deformation yields less increase in hardness on the top (less than two times the base). Importantly, the observed hardness profiles signify that the GS steepness does not change as a monotonic function of the temperature (in the surveyed range between 300 K and 673 K) for surface severe deformation.

The overview of the GS formed at different temperatures is presented in Fig. 2b–d using EBSD inverse pole figure (IPF) mapping, showing a slightly increased influential depth upon deformation as processing temperature increases. Note the microstructure of the topmost layer is not properly resolved due to the resolution limit of EBSD (gray bands). Nevertheless, understanding this layer of GS becomes the key to deciphering the temperature effect on the GS steepness. Fig. 2e–j demonstrate the bright-field (BF) TEM micrographs in conjunction with PED-based orientation maps of the Al phase in the specimens lifted out from the top 10 μm of the GS processed at three temperatures. The dynamical recrystallization is substantiated by the high-angle grain boundary features in IPF maps. The equilibrium recrystallization grain size (d) increases as temperature rises (Table 1), driven by the reduction of grain boundary energy. It is safe to conclude a gradual loss of grain boundary strengthening in the GS as processing temperature increases. Therefore, given the highest surface hardness at the intermediate temperature, another strengthening factor must be present to play a larger role. Notably, the grain contrast under BF imaging is much sharper for the room-temperature specimen but becomes blurred for the elevated-

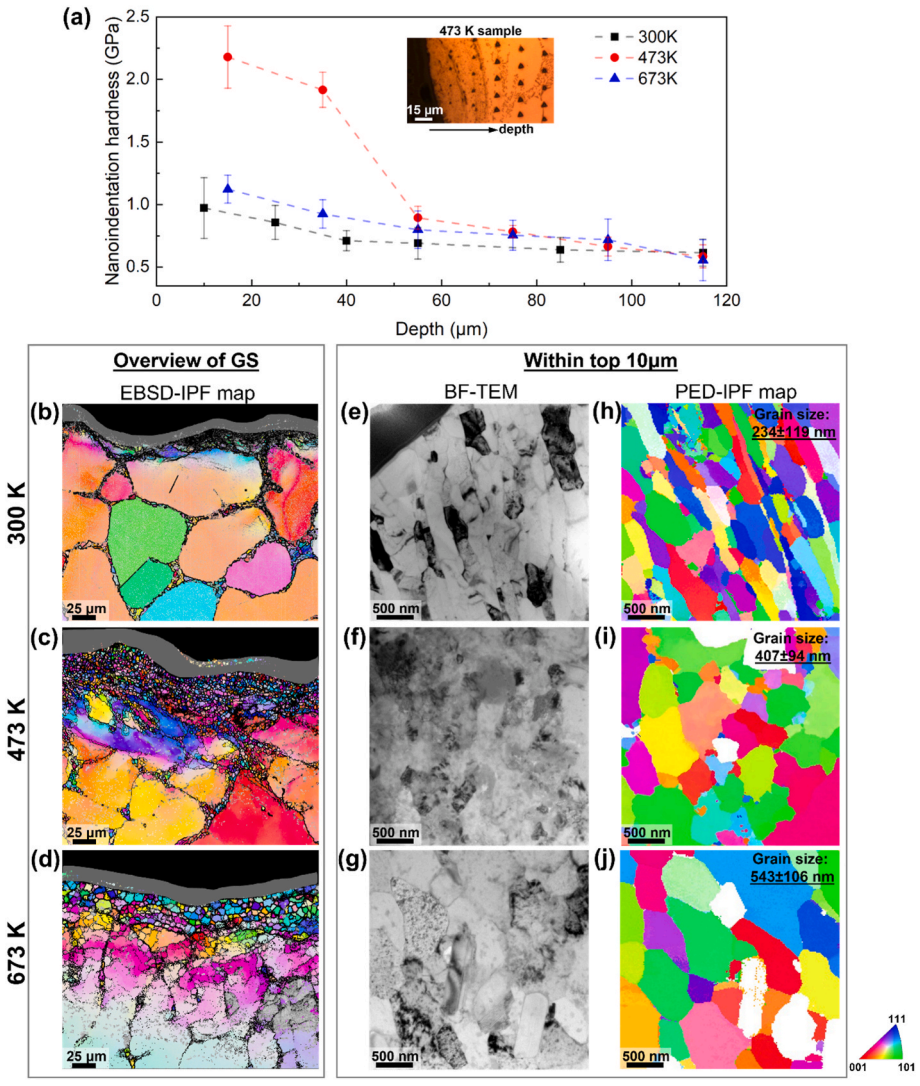

Fig. 2. (a) Nanoindentation hardness profiles to characterize the GS steepness obtained at three temperature conditions. The inset is an optical micrograph showing the indent arrays on the GS produced by the surface severe deformation at 473 K; (b, c, d) Overview microstructures of GS using EBSD, Grey bands represent the regions that are not resolved by EBSD; (e, f, g) BF-TEM micrographs and (h, i, j) PED IPF maps of microstructures in the top 10 μm layer of GS obtained at three different temperatures (300K, 473K, 673 K).

Table 1
Statistics of grain size, oxide size, spacing, and density & strengthening analysis in the top layer (10 μm) of GS produced at different temperatures.

	300 K	473 K	673 K
Grain size d (nm)	234 ± 119	407 ± 94	543 ± 106
Oxide radius r (nm)	N/A	23 ± 12	20 ± 10
Oxide spacing L (nm)	N/A	116 ± 33	188 ± 57
Number density ($\times 10^{11}$ mm^{-3})	N/A	6.4 ± 2.5	1.5 ± 0.6
Hall-Petch strengthening $\Delta\sigma_{HP}$ (MPa)	163	124	107
Orowan strengthening $\Delta\sigma_{Orowan}$ (MPa)	N/A	302	144
Sum of Hall-Petch and Orowan strengthening (MPa)	163	426	251

temperature counterparts (Fig. 2e–g), although all of them are dominated by high-angle grain boundaries (as shown in the PED-IPF maps). This difference indicates the probable emergence of oxide particles during deformation at elevated temperatures, complicating the diffraction contrast for BF imaging.

To confirm the oxide particles and their distribution at three conditions, STEM EDS and APT analyses were further performed on specimens prepared from a region within the top 10 μm layer of GS. The element distribution patterns distinctively differ from one processing temperature to another. At 300 K, the silicon-rich eutectic phase was effectively refined and became primarily decorated at the Al grain boundaries, the details of which have been investigated elsewhere [18]. Notably, the oxygen signal was weak and did not show any cluster patterns, i.e., no substantial formation of oxides during room-temperature deformation. At 473 K, fragmentation of the silicon-rich eutectic phase was still

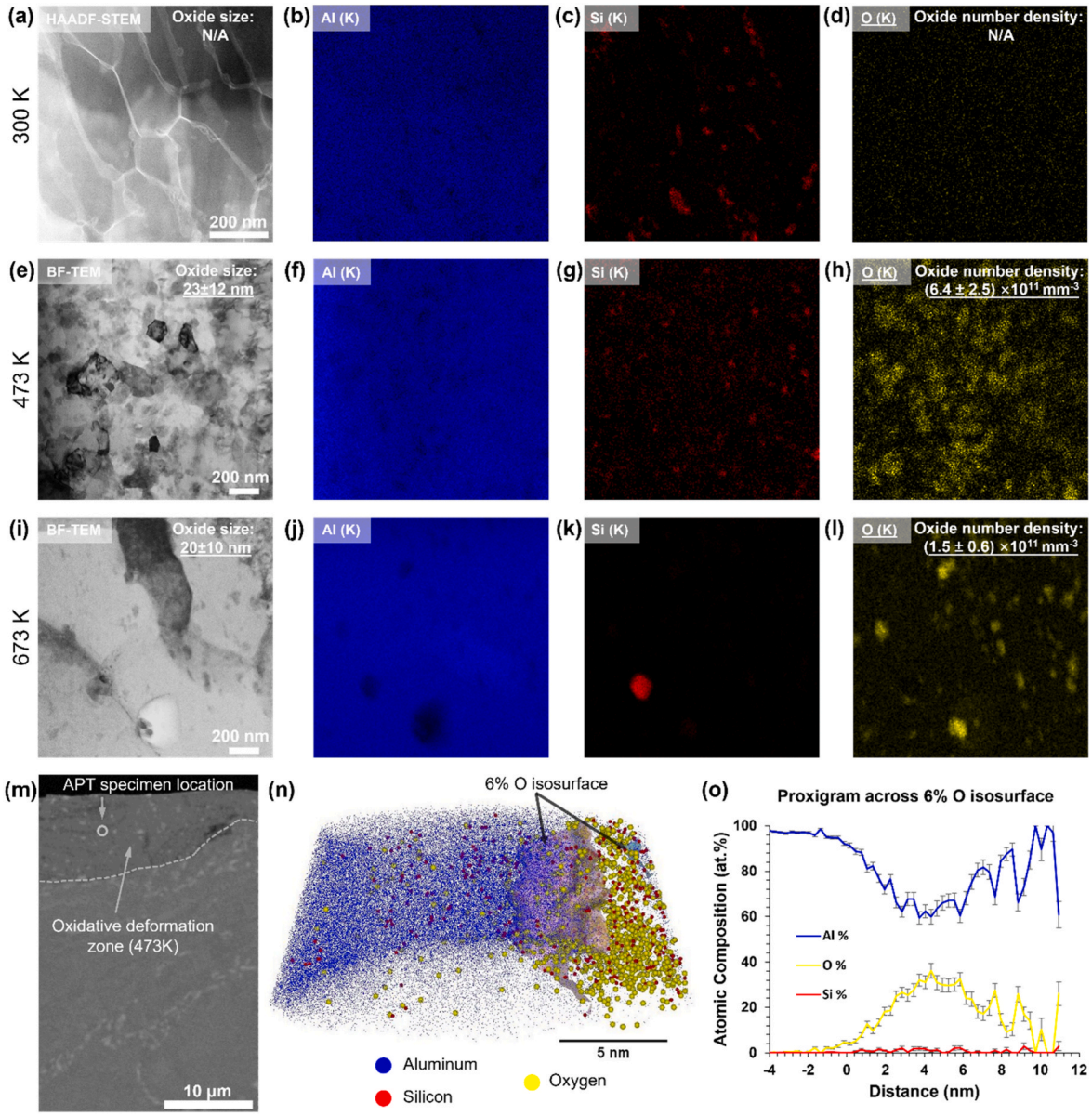

Fig. 3. EDS maps of microstructure within the top 10 μm layer of GS produced at (a-d) 300 K; (e-h) 473 K; and (i-l) 673 K to reveal the elemental distribution of Al, Si, and O. (m) backscatter electron micrograph of the GS produced at 473 K. The open circle marks the location of specimen for APT analysis. (n) 3D reconstruction of the evaporated specimen, highlighting Al (blue), Si (red), and O (yellow) in the volume; (o) Proximity histogram of atomic concentration profiles across the large 6 at % O isosurface in (n), where the center reveals an aluminum oxide particle. Note that the exact stoichiometry between Al and O needs to further take into account the O deficiency in the APT analysis due to the multiple hit and peak overlap [23]. (For interpretation of the references to colour in this figure legend, the reader is referred to the Web version of this article.)

present (Fig. 3g). Strikingly, profuse oxide particles were identified by the oxygen map at the same time (Fig. 3h). One such particle was further captured and validated as an aluminum oxide in the APT specimen. The isoconcentration surface of 6 at.% O was used to delineate the boundary of such oxide enriched region in Fig. 3n. A proximity histogram analysis [19] was performed for the large interface located at the center of the APT needle. The analysis is similar to a 1D composition profile that follows the contour of the selected surface. Fig 3o shows oxide region (positive x axis) is enriched with Al element, indicating the formation of aluminum oxide. Moving to 673 K, refinement of silicon-rich phase became less common, and the aluminum oxides were observed but with a much lower density compared to the case at 473 K. The comparison of oxide number density at 473 K and 673 K can be clearly corroborated by the tilting BF movies near the boundary of oxidative deformation zone, in which oxide particles become small, dispersed, and twinkling spots (Movie 1 and 2). We closely examined the EDS maps and the BF movies by counting and measuring the oxides in the view field and concluded their radius (r) and spacing (L) of oxides, as summarized in Table 1. While the oxide particles at 473 K and 673 K are statistically close in size, the effective spacing (L-2r) of the former is half of the latter.

Supplementary video related to this article can be found at https://doi.org/10.1016/j.msea.2022.144061

For the rest of the manuscript, we will proceed with two critical issues: first, elucidating the decisive role of oxide particles in the strengthening of the top layer, i.e., in manipulating the GS steepness; second, explaining why the densest oxide dispersion, i.e., GS steepness, is attained at the intermediate temperature, rather than the higher or the lower.

Considering the strengthening effect in the top layer (10 μm) of GS, two primary factors are responsible: grain boundaries (Hall-Petch strengthening) and oxide dispersion (Orowan strengthening). The two strengthening effects can be estimated using the following two equations, respectively [20–22]:

$$\Delta\sigma_{HP} = kd^{-1/2} \tag{1}$$

$$\Delta\sigma_{Orowan} = \frac{MGb}{L-2r} \tag{2}$$

where k is the Hall-Petch coefficient for Al–Si alloy, 2.5 MPa mm$^{1/2}$ [24]; M is Taylor factor for polycrystalline materials, 3 for face-centered cubic metals; G is shear modulus, 26 GPa; b is Burger vector, 0.286 nm.

We note the fragmented silicon phase also provides strengthening, especially for 300 K and 473 K. However, it appears second to the oxides given its primary residence at grain boundaries and lower density (Fig. 3g), and an early report found its effect is even much lower than grain boundaries [18]. Given the negligible lattice friction stress in Al ($\sigma_0 \cong 10$ MPa), the calculations (in Table 1) yield a reasonable agreement with the trend of nanoindentation hardness measurement of the top layers in three samples (Fig. 2). The analysis suggests the oxides dispersion strengthening indeed dictates the high hardness of the top layer of GS at the intermediate temperature.

The counterintuitive attainment of the densest oxide dispersion at the intermediate temperature could be understood by the dynamic interplay between cyclic tribological deformation and the surface oxidation as a function of temperature, as sketched in Fig. 4. On one hand, the susceptibility of the Al phase to thermal oxidation increases as temperature rises due to the enhanced kinetics for the reaction [25]. For thermal oxidation, the aluminum oxide growth rate complies with the Mott-Cabrera model below under static reaction [25]: $\frac{dx}{dt} = A\exp\left(-\frac{Q}{kT}\right)$; where x is the oxide layer thickness in static reaction and can be interpreted as the oxide dispersoid density in our case since the overall oxide volume fraction is low; t is time; A is pre-factor constant for the reaction; Q is the energy barrier; k is the Boltzmann constant, and T is temperature. Clearly, for a given time, the attained oxide density increases as temperature. Meanwhile, the mechanical loading is expected to further aid the oxidation by mechanical-induced mass transport [26,27], which explains why oxidative deformation zone is observed in our 473 K specimen under severe deformation but not evidenced in static oxidation under the same temperature in the literature [25,28].

On the other hand, thermal softening at elevated temperatures leads to an increased wear loss of the pre-oxidized layer (Fig. 1), giving rise to the diminishing ability to retain and accumulate the oxide dispersion upon cyclic tribological deformation. For wear loss, one can consider the Archard's wear equation [29]: $= K_{wear}\frac{WS}{H(T)}$; where V is the total volume of wear debris during tribological deformation; K_{wear} is a dimensionless constant; W is the load; S is sliding distance; H is the material hardness and depends on the deforming temperature T. Rising temperature lowers the barriers to dislocation slip, leading to lower hardness. Thus, it can be anticipated that the total material loss is higher at elevated temperatures. The material loss during deformation means the obtained oxide dispersion in early stages is lost, countering the accumulation of

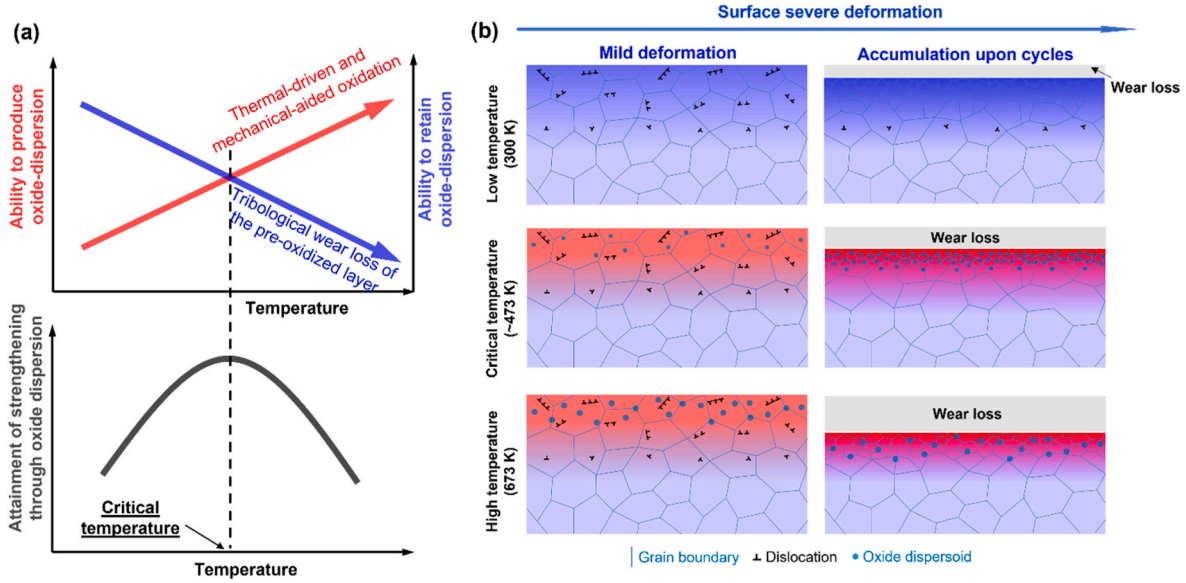

Fig. 4. (a) Schematics of how the interplay between surface oxidation and wear loss affect the ability to produce/retaining oxide-dispersion surface during surface severe deformation as a function of temperature; (b) Graphic illustration of formation and evolution of surface layer in GS under different temperature conditions.

oxide dispersion owing to thermal oxidation.

Consequently, there exists a critical temperature to produce the oxide-dispersion strengthening to its maximum potential along with recrystallization-induced refinement by progressive accumulation to a dynamic saturation (Fig. 4b). Above this critical temperature, gaining oxide-dispersion strengthening becomes ineffective due to the significant wear loss of surface layers containing oxides formed precedently. The sparse oxide particles observed in the 673 K specimen were presumably generated during the last few cycles of deformation. In our study, this critical or "sweet point" temperature for Al–Si alloy to attain the steepest GS is substantiated by the non-monotonic trend of the obtained GS steepness as a function of temperature between 300 K and 673 K.

4. Summary

In closing, we studied the GS formation in Al-4at.% Si alloy by surface severe deformation under various temperatures. A steeper gradient is surprisingly obtained at the intermediate temperature owing to the *in situ* formation and dispersion of oxide particles in its top layer. A detailed microstructural characterization reveals that the oxide-dispersion influences the steepness of the GS under different temperatures. The high-density (6.4×10^{11} mm^{-3}) and narrow spacing of fine-scale oxide dispersoids are not observed at the lower or higher temperature processing conditions. The counterintuitive attainment of a steeper GS at the intermediate temperature is explained by the dynamic interplay between oxidation susceptibility and tribological material loss as a function of temperature. Consequently, there is a critical temperature to produce and retain the oxide dispersion along with grain refinement for effective strengthening. The observation is not anticipated to be limited to the Al alloy and is potentially applicable to other metallic materials when designing and fabricating GS using surface attrition- or wear-based processing techniques.

Originality Statement

I write on behalf of myself and all co-authors to confirm that the results reported in the manuscript are original and neither the entire work, nor any of its parts have been previously published. The authors confirm that the article has not been submitted to peer review, nor has been accepted for publishing in another journal. The author(s) confirms that the research in their work is original, and that all the data given in the article are real and authentic. If necessary, the article can be recalled, and errors corrected.

CRediT authorship contribution statement

Xiaolong Ma: Conceptualization, Methodology, Formal analysis, Investigation, Writing – original draft, Writing – review & editing. **Matthew Olszta:** Methodology, Formal analysis, Investigation, Writing – review & editing. **Jia Liu:** Methodology, Formal analysis, Investigation, Writing – review & editing. **Miao Song:** Methodology, Investigation, Writing – review & editing. **Mayur Pole:** Methodology, Formal analysis, Investigation, Writing – review & editing. **Madhusudhan R. Pallaka:** Methodology, Formal analysis, Investigation, Writing – review & editing. **Joshua Silverstein:** Methodology, Investigation. **Julian Escobar:** Methodology, Formal analysis, Writing – review & editing. **Arun J. Bhattacharjee:** Methodology, Formal analysis, Investigation. **Sundeep Mukherjee:** Resources, Writing – review & editing. **Arun Devaraj:** Resources, Writing – review & editing. **Bharat Gwalani:** Conceptualization, Methodology, Formal analysis, Investigation, Writing – review & editing.

Declaration of competing interest

The authors declare that they have no known competing financial interests or personal relationships that could have appeared to influence the work reported in this paper.

Data availability

Data will be made available on request.

Acknowledgments

This research was supported by the SPPS (Solid Phase Processing Science) Initiative at the Pacific Northwest National Laboratory, USA. The authors are grateful to Anthony Guzman for the preparation of specimens for microstructural characterization, and Professor Mathaudhu Suveen for advice. The Pacific Northwest National Laboratory is operated by Battelle for the U.S. Department of Energy under contract DE-AC06-76101830.

Appendix A. Supplementary data

Supplementary data to this article can be found online at https://doi.org/10.1016/j.msea.2022.144061.

References

[1] S. Suresh, Graded materials for resistance to contact deformation and damage, Science 292 (2001) 2447–2451, https://doi.org/10.1126/science.1059716.
[2] T.H. Fang, W.L. Li, N.R. Tao, K. Lu, Revealing extraordinary intrinsic tensile plasticity in gradient nano-grained copper, Science 331 (2011) 1587–1590, https://doi.org/10.1126/science.1200177.
[3] X. Li, L. Lu, J. Li, X. Zhang, H. Gao, Mechanical properties and deformation mechanisms of gradient nanostructured metals and alloys, Nat. Rev. Mater. 5 (2020) 706–723, https://doi.org/10.1038/s41578-020-0212-2.
[4] Z. Cheng, H. Zhou, Q. Lu, H. Gao, L. Lu, Extra strengthening and work hardening in gradient nanotwinned metals, Science 362 (2018), https://doi.org/10.1126/science.aau1925 eaau1925.
[5] L. Zhu, H. Ruan, A. Chen, X. Guo, J. Lu, Microstructures-based constitutive analysis for mechanical properties of gradient-nanostructured 304 stainless steels, Acta Mater. 128 (2017) 375–390, https://doi.org/10.1016/j.actamat.2017.02.035.
[6] Q. Pan, L. Zhang, R. Feng, Q. Lu, K. An, A.C. Chuang, J.D. Poplawsky, P.K. Liaw, L. Lu, Gradient cell–structured high-entropy alloy with exceptional strength and ductility, Science 374 (2021) 984–989, https://doi.org/10.1126/science.abj8114.
[7] X.L. Wu, P. Jiang, L. Chen, J.F. Zhang, F.P. Yuan, Y.T. Zhu, Synergetic strengthening by gradient structure, Mater. Res. Lett. 1–7 (2014), https://doi.org/10.1080/21663831.2014.935821.
[8] T. Roland, D. Retraint, K. Lu, J. Lu, Fatigue life improvement through surface nanostructuring of stainless steel by means of surface mechanical attrition treatment, Scripta Mater. 54 (2006) 1949–1954, https://doi.org/10.1016/j.scriptamat.2006.01.049.
[9] X. Chen, Z. Han, X. Li, K. Lu, Lowering coefficient of friction in Cu alloys with stable gradient nanostructures, Sci. Adv. 2 (2016), e1601942, https://doi.org/10.1126/sciadv.1601942.
[10] J. Li, A.K. Soh, Modeling of the plastic deformation of nanostructured materials with grain size gradient, Int. J. Plast. 39 (2012) 88–102, https://doi.org/10.1016/j.ijplas.2012.06.004.
[11] X. Yang, X. Ma, J. Moering, H. Zhou, W. Wang, Y. Gong, J. Tao, Y. Zhu, X. Zhu, Influence of gradient structure volume fraction on the mechanical properties of pure copper, Mater. Sci. Eng. 645 (2015) 280–285.
[12] X. Wu, Y. Zhu, Heterogeneous materials: a new class of materials with unprecedented mechanical properties, Mater. Res. Lett. 5 (2017) 527–532, https://doi.org/10.1080/21663831.2017.1343208.
[13] Y. Lin, J. Pan, H.F. Zhou, H.J. Gao, Y. Li, Mechanical properties and optimal grain size distribution profile of gradient grained nickel, Acta Mater. 153 (2018) 279–289, https://doi.org/10.1016/j.actamat.2018.04.065.
[14] X. Ma, C. Huang, J. Moering, M. Ruppert, H.W. Höppel, M. Göken, J. Narayan, Y. Zhu, Mechanical properties of copper/bronze laminates: role of interfaces, Acta Mater. 116 (2016) 43–52.
[15] Y. Zhu, Introduction to heterostructured materials: a fast emerging field, Metall. Mater. Trans. (2021), https://doi.org/10.1007/s11661-021-06438-8.
[16] C. Liu, Z. Li, W. Lu, Y. Bao, W. Xia, X. Wu, H. Zhao, B. Gault, C. Liu, M. Herbig, A. Fischer, G. Dehm, G. Wu, D. Raabe, Reactive wear protection through strong and deformable oxide nanocomposite surfaces, Nat. Commun. 12 (2021) 5518, https://doi.org/10.1038/s41467-021-25778-y.
[17] V.S. Zolotorevskii, N.A. Belov, M. Glazoff, Casting Aluminum Alloys, Elsevier, Amsterdam; Boston; London, 2007.
[18] B. Gwalani, M. Olszta, S. Varma, L. Li, A. Soulami, E. Kautz, S. Pathak, A. Rohatgi, P.V. Sushko, S. Mathaudhu, C.A. Powell, A. Devaraj, Extreme shear-deformation-induced modification of defect structures and hierarchical microstructure in an Al–Si alloy, Commun. Mater. 1 (2020) 85, https://doi.org/10.1038/s43246-020-00087-x.

[19] O.C. Hellman, J.A. Vandenbroucke, J. Rüsing, D. Isheim, D.N. Seidman, Analysis of three-dimensional atom-probe data by the proximity histogram, Microsc. Microanal. 6 (2000) 437–444, https://doi.org/10.1007/S100050010051.
[20] E.O. Hall, The deformation and ageing of mild steel: III discussion of results, Proc. Phys. Soc. B 64 (1951) 747–753, https://doi.org/10.1088/0370-1301/64/9/303.
[21] N.J. Petch, The cleavage strength of polycrystals, J. Iron Steel Inst. 174 (1953) 25–28.
[22] E. Orowan, Symposium on Internal Stresses in Metals and Alloys, Session III Discussion, Institute of Metals, London, England, 1948.
[23] A. Devaraj, R. Colby, W.P. Hess, D.E. Perea, S. Thevuthasan, Role of photoexcitation and field ionization in the measurement of accurate oxide stoichiometry by laser-assisted atom probe tomography, J. Phys. Chem. Lett. 4 (2013) 993–998, https://doi.org/10.1021/jz400015h.
[24] R.W. Armstrong, Hall–Petch relationship in aluminum and aluminum alloys, in: Encycl. Alum. Its Alloys, first ed., CRC Press, Boca Raton, 2019 https://doi.org/10.1201/9781351045636-140000234.
[25] L.P.H. Jeurgens, W.G. Sloof, F.D. Tichelaar, E.J. Mittemeijer, Growth kinetics and mechanisms of aluminum-oxide films formed by thermal oxidation of aluminum, J. Appl. Phys. 92 (2002) 1649–1656, https://doi.org/10.1063/1.1491591.
[26] Z. Liu, C. Patzig, S. Selle, T. Höche, P. Gumbsch, C. Greiner, Stages in the tribologically-induced oxidation of high-purity copper, Scripta Mater. 153 (2018) 114–117, https://doi.org/10.1016/j.scriptamat.2018.05.008.
[27] X. Chen, Y. Ma, Y. Yang, A. Meng, Z.X. Han, Z. Han, Y.H. Zhao, Revealing tribo–oxidation mechanisms of the copper–WC system under high tribological loading, Scripta Mater. 204 (2021), 114142, https://doi.org/10.1016/j.scriptamat.2021.114142.
[28] H. S, Oxidation and kinetic analysis of pure aluminum powder under nonisothermal condition, J. Aquacult. Res. Dev. (2012), https://doi.org/10.4172/scientificreports.385, 01.
[29] J.F. Archard, Contact and rubbing of flat surfaces, J. Appl. Phys. 24 (1953) 981–988, https://doi.org/10.1063/1.1721448.